

1   **Controls on the Effect of Impact Scrapping on High-position and Long-runout**  
2   **Landslides**

3   Yang Gao<sup>a,b</sup>, Yueping Yin<sup>c,\*</sup>, Bin Li<sup>a,b,d</sup>, Haoyuan Gao<sup>d</sup>, Zhuang Li<sup>d</sup>

4

5   <sup>a</sup>*Institute of Geo-Mechanics, Chinese Academy of Geo-Sciences, CGS, China*

6   <sup>b</sup>*China University of Geosciences, Beijing, China*

7   <sup>c</sup>*China Institute of Geo-Environment Monitoring, Beijing, China*

8   <sup>d</sup>*Changan University, Shanxi, China*

9

10   \*Corresponding author at: Institute of Geo-Mechanics, Chinese Academy of  
11   Geo-Sciences, CGS, China.

12   E-mail address: 737263992@qq.com (Y Gao).

13

14   Ethical Statement:

15   I certify that this manuscript is original and has not been published elsewhere for  
16   publication while being considered. And the study is not split up into several parts to  
17   increase the quantity of submissions and submitted to various journals or to one journal  
18   over time. No data have been fabricated or manipulated (including images) to support  
19   your conclusions. No data, text, or theories by others are presented as if they were our  
20   own.

21   The submission has been received explicitly from all co-authors. And authors whose  
22   names appear on the submission have contributed sufficiently to the scientific work and  
23   therefore share collective responsibility and accountability for the results.

24

25 **F-ABSTRACT**

26 Landslides in mountainous areas act as an important control on morphological landscape  
27 evolution and represent a major natural hazard. The dynamic characteristics of a landslide  
28 directly relate to the distance it traveled and the scale of the resulting disaster. Based on  
29 extensive field investigations, we explored the effect of impact scraping on high-position  
30 landslides. During a rapid landslide, impact scraping amplifies the volume of the  
31 landslide and the size of the area affected by the landslide. Without acknowledging this  
32 effect, it is easy to underestimate the risk presented by a given potential landslide. In this  
33 study, we investigate the impact scraping of landslides that travel for significant distances  
34 both vertically (high-position) and horizontally (long-runout). There are four  
35 developmental stages of high-position, long-runout landslides: high-position shearing,  
36 gravitational acceleration, impact scraping, and debris deposition. Impact scraping  
37 amplifies the scale of the disaster by drastically increasing the volume of the landslide  
38 debris. After accounting for the effect of impact scraping, the total volume of the  
39 landslide exhibits a strong correlation with its travel distance. Additionally, the material  
40 properties of the erodible layer influence the landslide mobility. High-position and  
41 long-runout landslides have multiple scraping modes, including the embedding and  
42 excavation mode, the entrainment mode, the pushing and sliding mode, and the impact  
43 and splashing mode. In this study, we aim to provide insight that will improve the  
44 disaster modeling and risk assessment of high-position landslides, as well as to offer  
45 theoretical support for high-position and long-runout landslide dynamics research,  
46 disaster prevention and mitigation, and first responder rescue operation planning.

47 *Keywords:* Landslides, Impact scraping, High-position, Numerical simulation

48

49        **1. Introduction**

50        Landslides in mountainous areas act as an important control on morphological  
51        landscape evolution and represent a major natural hazard ([Bonnard, 2004; Crozier and](#)  
52        [Glade, 2005](#)). These landslides are influenced by factors such as topography, soil type,  
53        geological conditions, fractures, bedding planes, and moisture content ([Crozier, 1986;](#)  
54        [Turner and Schuster, 1996; Malamud et al., 2004](#)). High-position and long-runout  
55        landSliding main body Is a landslide that shears out from a high steep slope and forms an  
56        accelerating main body, where the elevation difference exceeds 350 m between toe of  
57        surface of rupture and toe of landslide([Zhang et al., 2014; Yin et al., 2017](#)). These  
58        landslides have a higher initial start-up position, a long-runout mobility distance, and a  
59        high impact    kinetic energy, threat to human beings, animal and fauna, and social and  
60        economic development. High-position and long-runout landSliding main body Involves  
61        the conversion of an enormous amount of potential energy into kinetic energy, this  
62        mobility process in which impact scraping plays a critical role. After a high position  
63        landslide failure, the dynamic contact between the sliding main body with the stability  
64        mountain, maybe leading to secondary landslide, changing the mobility state and forming  
65        a disaster chain reaction, which can easily lead to obvious error in risk prediction and  
66        judgment. Impact scraping effect often causes the landslide volume to increase by one to  
67        six times that of its initial volume, thereby multiplying the scale of the disaster and its  
68        ability to transform the surrounding landscape. For landslides that increase in volume,  
69        such as the 1970 Nevado Huascarán landSliding main body In Peru, sliding main body  
70        volume is enlarged 5.7 times to the initial volume ([Evans et al., 2009; Strom, 2014](#)), the

71 2013 Zhaojiagou landSliding main body In Zhenxiong, Yunnan, China, sliding main body  
72 volume is enlarged 1.5 times to the initial volume ([Xu et al., 2009; Yin, 2010; Zhang et](#)  
73 [al., 2014](#)), and the 2019 Jichang landSliding main body In Shuicheng, Guizhou, China,  
74 this landslide sliding main volume body is enlarged 2 times to the initial volume([Gao et](#)  
75 [al., 2020](#)). During the process of impact scraping, the integrated body constantly  
76 disintegrated to form debris body, and then transforms into long-runout landslide-debris  
77 flow, which increases the damage of landslide disaster and leads to mass death and injury.

78 In the early 20th century, [Stiny and Die \(1910\)](#) and [Heim \(1932\)](#) noted that dynamic  
79 scraping effects played a critical role about the mobility and deposition process of  
80 landslides-debris. Dynamic impact and scraping usually occurs at the front and lateral  
81 edges of a landslide, resulting in the creation of leading edge plows, splash zones, and  
82 scour marks. Like the "plow" shovel move the underlay and around it, and can often  
83 observe the "splash belt" and "scratches" formed after the shovel occurs. This contact  
84 process increases the volume and overall scale of the landslide([Hung, 2004; McDougall](#)  
85 [and Hung, 2005](#)). There are different terms to describe dynamic scraping process in  
86 landslide ([Takahashi, 1978; Hung, 2004; Sovilla et al., 2006; Crosta et al., 2009; Iverson,](#)  
87 [2012; Zhou et al., 2016](#)). "Scraping" generally refers to dynamic contact, "entrainment"  
88 and "scouring" are mostly used to express the erosion at the bottom of the debris flow,  
89 and "impact," "plow," and "push" are commonly used to describe the impact and  
90 impingement at the leading edges of flowing bodies such as landslides, avalanche, and  
91 debris flows. Because it is difficult to record and capture during the landslide dynamic  
92 scraping process. In order to better restore and analyze the scraping process, statistical  
93 analyses, chute model test and numerical simulation methods have become the most

94 effective research means.

95 Statistical analyses of landslide characteristics can yield valuable insight into  
96 landslide prediction and risk mitigation. Landslide size is a strong predictor of runout  
97 distance in a variety of different landslide types (Legros, 2002; Roback et al., 2018).  
98 Because the reach angles tend to be lower for large landslides than they are for smaller  
99 landslides, the resulting landslides are considered more mobile (Scheidegger, 1973; HsÜ,  
100 1975; Lucchitta, 1978; Li, 1983; Voight et al., 1983). There is a correlation between the  
101 volume of the slide and the tangent of the reach angle, which is expressed as the ratio  
102 between the vertical drop distance,  $H$ , and the horizontal projection of the runout distance,  
103  $L$  (Guzzetti et al., 2009; Brunetti et al., 2014; Iverson et al., 2015). It is necessary to  
104 further investigate impact scraping effect as it leads to increase in the landslide volume  
105 and therefore directly influences landslide mobility process and the tangent of the reach  
106 angle.

107 Chute model tests are scale models that recreate the mobility and deposition in  
108 landslides dynamic processes for the purposes of establishing mechanical models that  
109 allow the user to fully investigate the various impact scraping patterns (Savage and  
110 Hutter, 1991; Iverson, 2011; Dufresne, 2012). Previous chute model tests have revealed  
111 that the slide angle and the material properties of the eroded layer affect the mobility and  
112 the deposition modes of a landslide (Mangeney et al., 2010; Zhou et al., 2016).

113 Numerical simulations are the most efficient method of studying the impact scraping  
114 effect in high-position landslides. At present, there are many numerical methodologies  
115 that account for impact scraping effect in the landslide dynamic process. For example, a  
116 numerical simulation method based on the law of continuum mechanics, which is an

117 efficient computational method based on the equivalent fluid theory of landslide mobility,  
118 include the lattice Boltzmann method (LBM), the smoothed grain hydrodynamics (SPH)  
119 method, and the material point method (MPM) (McDougall and Hungr, 2005; Crosta et  
120 al., 2009; Pirulli and Pastor, 2012; Huang et al., 2014; Xing et al., 2014). A numerical  
121 simulation method based on the mechanical law of the discrete media, which is a type of  
122 computational method based on non-continuum mechanics and contact mechanics,  
123 include PFC, EDEM, DDA, and MatDEM (Li et al., 2012; Zhang et al., 2012; Liu et al.,  
124 2017; Wang et al., 2017; Li et al., 2018, Huang, et al. 2018, 2019; Song, et al. 2016).

125 The discrete element method is capable of simulating deformation at various scales,  
126 different contact types, and a range of friction coefficients, which can simulate large  
127 deformation, suitable for the numerical inversion analysis of the impact scraping effect of  
128 debris avalanche and debris flow. These numerical simulation methods, which rely on the  
129 selection of suitable model parameters, avoid the disadvantages of chute model tests (e.g.,  
130 operational difficulties and the size effect of landslides) while yielding highly  
131 reproducible results.

## 132 **2. Method**

133 We used a variety of methods to quantify the degree of influence exerted by impact  
134 scraping on landslide mobility characteristics. From field surveys, we collected site  
135 photographs and topographic data both before and after multiple landslides. Additionally,  
136 we conducted statistical analyses using parameters such as the eroded volume and the  
137 landslide mobility index to determine if the landslide mobility characteristics are related  
138 to any specific impact scraping responses. Lastly, we used numerical simulations to  
139 recreate the impact scraping modes of high-position and long-runout landslides with

140 different underlayer materials.

141 *2.1. Field investigation and landslide characteristics*

142 Impact scraping typically occurs at the leading and side edges of a landslide,  
143 resulting in the aforementioned plow, splash zones, and scour marks ([Hungr, 2004](#);  
144 [McDougall and Hungr, 2005](#)). Because it may be difficult to find scraping traces in field  
145 surveys due to the presence of overlying depositional bodies, most of our field data  
146 consists of information about the terrain conditions both before and after a given  
147 landslide. First, we use field data and digital terrain (digital elevation model (DEM)) data  
148 to compare the topography of a given landSliding main body Impact area both before and  
149 after a landslide to determine the extent of the scraping. Then, we look at field survey  
150 data that capture scour traces at the boundary of the scour. Finally, we establish a  
151 generalized landslide mobility model by considering the common characteristics of most  
152 high-position landslides.

153 A well-known index that expresses the landslide mobility is the angle of the line  
154 connecting the head of the landslide source and the distal margin of the displaced mass  
155 ([Corominas, 1996](#); [Brideau et al., 2019](#); [Fan et al., 2019](#)). This angle is referred to as the  
156 angle of reach (fahrböschung angle) ([Heim, 1932](#)) or the equivalent friction coefficient  
157 ([Shreve, 1968](#)). Due to the relative scarcity of available landslide scraping data, we  
158 combined our photographic data with data from previous studies to examine a total of 15  
159 rapid and long-runout landslides with notable scraping characteristics. Ten of these  
160 landslides occurred in the mountainous areas of southwest China. From this data set, we  
161 collected information related to the landslide volume, the eroded volume, the total  
162 volume of the landslide, the mobility distance, the equivalent coefficient of friction, and

163 the scraping ratio. The volume of the sliding main body ( $V_m$ ) is that are initially failure  
164 during the deformation process, the mobility distance ( $L$ ) is the horizontal distance  
165 traveled, the equivalent coefficient of friction ( $\Delta H/L$ ) is the ratio of the line connecting  
166 the head of the landslide source to the distal margin of the displace mass, and the eroded  
167 volume ( $V_s$ ) is the increase in the landslide volume after the surrounding immobile rock  
168 and soil is eroded by the mobility of the landslide. Using statistical analyses, we  
169 determine the strength of the relationships between the pre- and post-scraping landslide  
170 volumes, the landslide runout distance, and the tangent of the reach angle.

171 *2.2. Numerical modeling methods*

172 Because it is difficult to record instances of impact scraping during a landslide,  
173 numerical simulations are the most efficient and effective techniques for recreating and  
174 observing the relationship between impact scraping and the mobility and depositional  
175 characteristics of landslide debris flows. We use the discrete element method to simulate  
176 and analyze the mobility of the underlayer and the landslide. The discrete element  
177 method, which is based on the principles of molecular dynamics, was developed by  
178 Cundall (1971) to analyze discrete granular materials. In this mathematical model, each  
179 grain is individually modeled as a single grain element with specified physical properties.  
180 Additionally, each grain is in a state of contact or separation with adjacent grains. When  
181 grains are in contact with one another, the magnitudes of the contact forces and moments  
182 are determined using either the Hertz-Mindlin contact model (Hertz, 1882; Mindlin, 1949;  
183 Mindlin and Deresiewicz, 1953; Cundall and Strack, 1979) or the Hertz-Mindlin with  
184 bonding contact model (Potyondy and Cundall, 2004). Both models are suitable for  
185 simulating the contact in concrete and rock structures.

186 Our numerical simulations consist of three underlayers of saturated soil (Underlayer  
187 I), hard soil (Underlayer II), and hard bedrock (Underlayer III), as well as a debris grain  
188 material (Sliding main body I) and a rock block slide (Sliding main body II) (Table 1).  
189 Using the Hertz-Mindlin contact model (used in underlayer I, underlayer II and Sliding  
190 main body I) and Hertz-Mindlin with bonding contact model (used in underlayer III and  
191 sliding main body II) to determine the parameters and the physical and mechanical  
192 properties of the three underlayers and two slides, we then conducted triaxial shear tests  
193 to ensure that the materials in our model simulations react realistically and produce  
194 robust and reliable results.

195

196 **Table 1**

197 Numerical chute simulations.

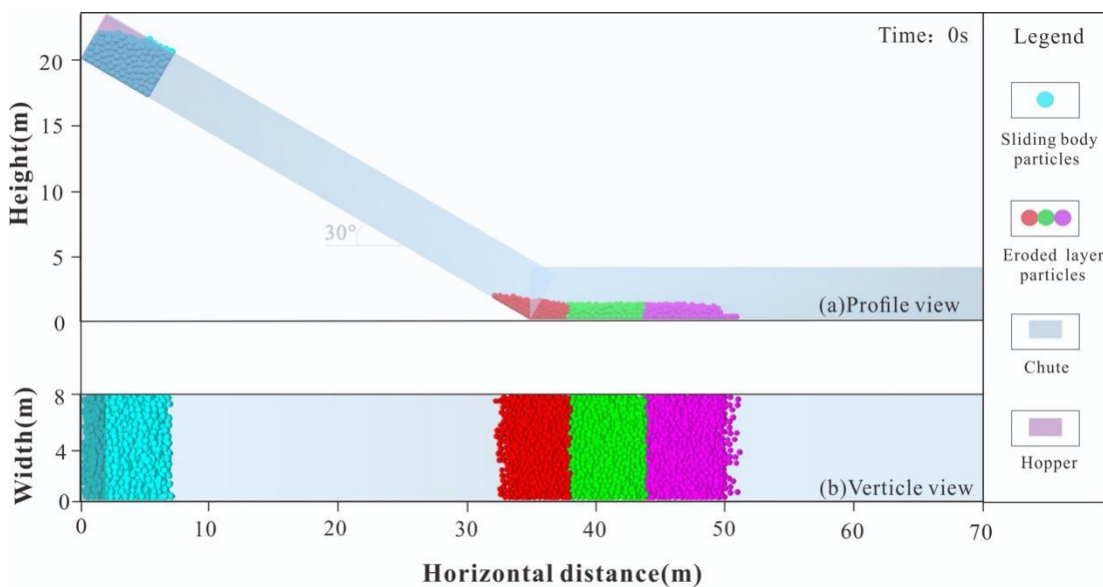
Numerical test material	Sliding main body I (Debris grains)	Sliding main body II (Limestone blocks)
Underlayer I	Test-01	Test-04
Underlayer II	Test-02	Test-05
Underlayer III	Test-03	Test-06

198

199 To simulate the dynamic characteristics of the effect of impact scraping for the two  
200 types of slides with three different scraping materials, we developed an inversion model  
201 based on the results of the landslide chute experiments. Our model consists of a  
202 two-section chute. The front section of the chute has an inclination of 0° and dimensions  
203 of 35 m × 8 m × 4 m (length × width × height). Within this section of the chute, we added

204 a 2 m thick layer of one of the three underlayer materials (Underlayer I, II, or III). The  
205 rear section of the chute has an inclination of 30° and dimensions of 40 m × 8 m × 4 m  
206 (Fig. 1). We conducted six landslide mobility experiments, representing each possible  
207 configuration for one type of initial sliding main body material and one underlayer. By  
208 adding the experimental constraints into our inversion model, we were able to gain  
209 valuable insight into the degree to which the underlayer materials and the sliding main  
210 body material affect the impact scraping modes.

211



212

213 **Fig. 1.** Schematic diagram of the chute configuration in our numerical simulations.

214

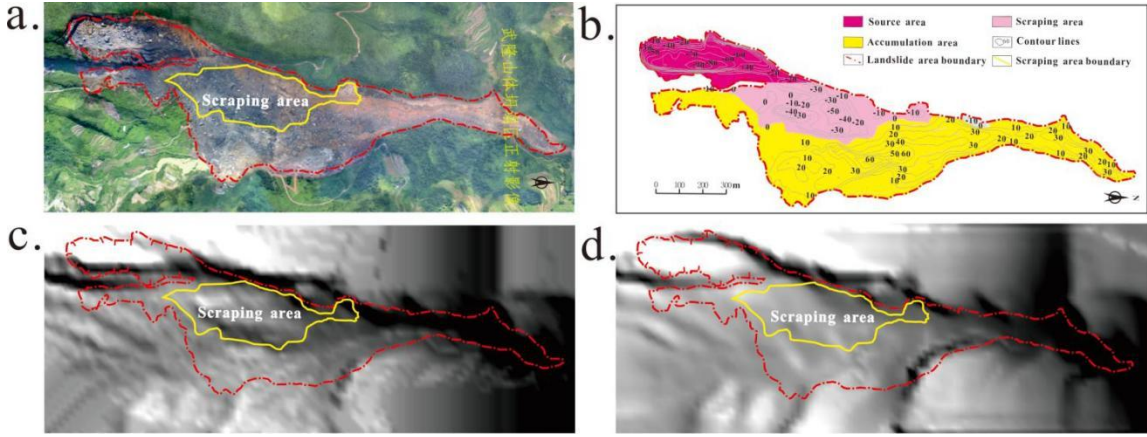
215 **3. LandSliding main body Impact scraping data from the Jiweishan landslide,**  
216 **China**

217 The Jiweishan landslide, which occurred on June 5, 2009, is notable for its rapid  
218 failure and long runout. A total carbonate volume of  $5 \times 10^6$  m<sup>3</sup> sheared out at a high  
219 position, causing landslide to collect an additional 600,000 m<sup>3</sup> of rocky hill material and

220 150,000 m<sup>3</sup> from a surface residual layer below the shear outlet. As a result, a  
221 considerable amount of initially intact rock and soil was damaged during the impact, and  
222 eventually joined the sliding main body material as it moved downstream along the  
223 Tiejiang gully. Continuous collision and disintegration of the landslide created a  
224 landslide-debris flow that ultimately deposited  $7 \times 10^6$  m<sup>3</sup> of landsliding main body  
225 material (the fractional amount of volume expansion due to fragmentation is 0.25) and  
226 caused 74 deaths ([Yin, 2010; Zhang et al., 2019](#)).

227 The deposition area of the Jiweishan landslide had a long, trumpet-shaped geometry  
228 with a length of ~2200 m along the gully, a maximum width of 470 m across the gully,  
229 and covered an area of  $\sim 46.8 \times 10^4$  m<sup>2</sup> (Fig. 2a). The deposition area can be divided into a  
230 landslide scraping zone and a debris flow deposition zone. The high-position sliding main  
231 body materials crossed the bottom of the gully and then rushed toward the opposite bank,  
232 where the flow was deflected so that it moved downstream along the gully. The average  
233 thickness of the deposition area is 30 to 40 m, with a maximum thickness of 60 m. The  
234 sliding main body material eventually collided with the mountain on the opposite bank,  
235 causing further disintegration of the sliding main body material and significant scraping  
236 of the mountain itself. As the slide blocks collided and disintegrated, they became part of  
237 a debris flow that moved more like a fluid than a solid mass. As the kinetic energy  
238 dissipated, the larger intact rocks were left behind in the main deposition area while high  
239 inertial forces drove the remaining sliding main body material, which consisted of  
240 material with relatively small grain sizes, to move forward in a streamlined, fluid state  
241 along the gully.

242

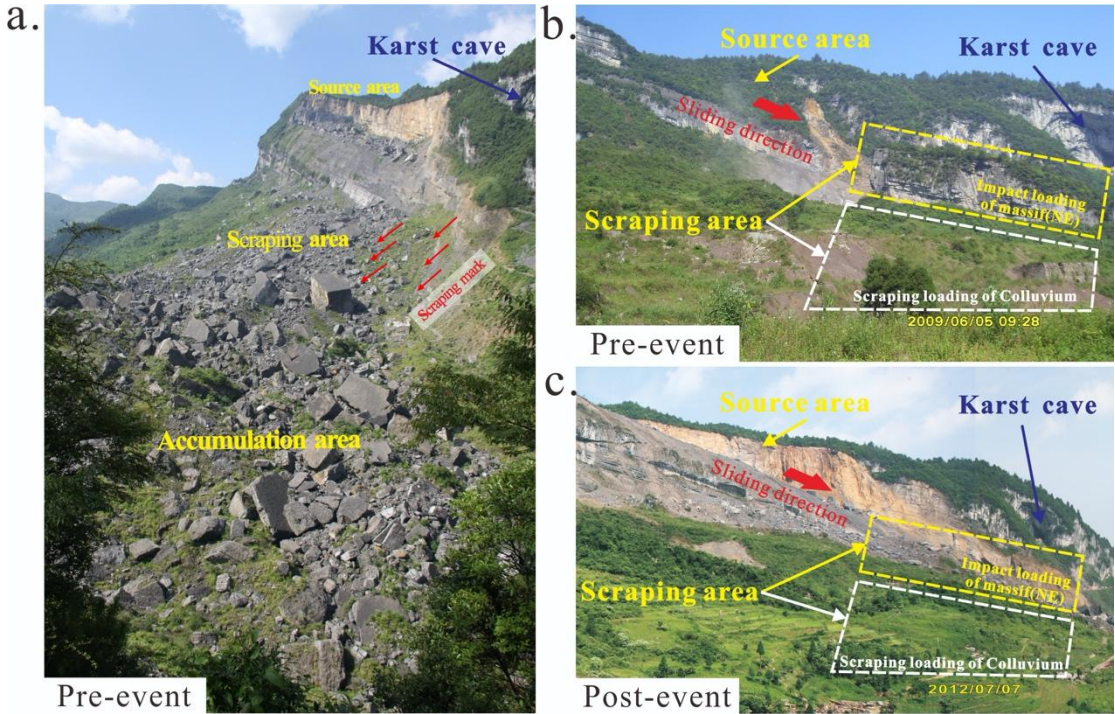


243  
244 **Fig. 2.** A typical example of a high-position and long-runout landslide exhibiting the  
245 impact scraping effect.

246 The elevation changes caused by the Jiweishan landslide are shown in Fig. 2b. The  
247 landslide eroded the immobile rock and soil beneath the shear outlet, forming a scraping  
248 zone with a maximum depth of 50 m and an area of  $\sim 14.3 \times 10^4$  m<sup>2</sup>. DEM data recorded  
249 before the landslide (Fig. 2c) indicates that this area originally hosted a significant  
250 protrusion that was almost entirely eroded away under by the landSliding main body  
251 Impact, leaving behind a notable scraping boundary (Fig. 2d).

252 In our detailed field investigations of the landslide scraping zone and the scraping  
253 boundary, we discovered scour marks at the slide boundary (Fig. 3a). A visual  
254 comparison of a photograph taken before the landslide (Fig. 3b) with a similar  
255 photograph taken after the landslide (Fig. 3c) shows that the slide eroded away a  
256 relatively significant protrusion on the downstream side of its shear outlet. There is also  
257 evidence that the landslide entrained and swept away the Quaternary residual slope debris  
258 in the scraping zone. Our field observations provide valuable constraints in our analysis  
259 of the effect of impact scraping.

260



261

262 **Fig. 3.** Field survey photographs taken (a, b) before and (c) after the Jiweishan landslide.

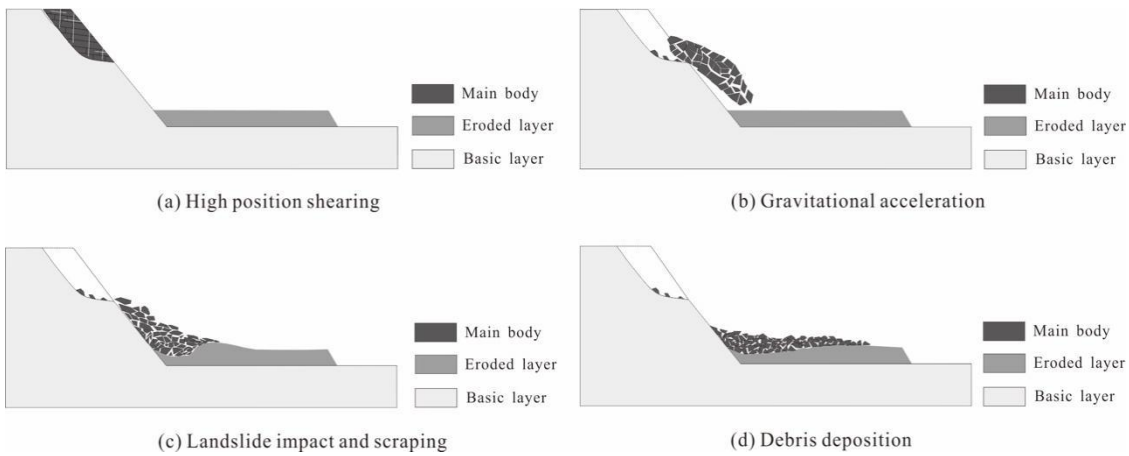
263

#### 264 **4. Landslide mobility features**

##### 265 *4.1. Landslide mobility*

266 Through the analysis of the records of several actual landslide cases (contain videos,  
 267 field investigation date, et al.), after the landslide blocks are initially destabilized, the  
 268 landslide progresses through four stages: high-position shearing, gravitational  
 269 acceleration, impact scraping, and debris deposition (Fig. 4). High-position and  
 270 long-runout landslides often prove disastrous to nearby plants, animals, and communities.

271



272

273 **Fig. 4.** The four evolutionary stages of a high-position long runout landslide, including (a)  
 274 high-position shearing, (b) gravitational acceleration, (c) landSliding main body Impact  
 275 and scraping, and (d) debris deposition.

276       High-position and long-runout landslides often develop in mountains with steep  
 277 terrain, intense cutting of rock mass discontinuities, and hard rock strata. High-position  
 278 shearing occurs when the elevation difference between the landslide shear outlet and the  
 279 leading edge of the deposition zone exceeds 350 m. This significant elevation difference  
 280 can pose logistical difficulties for those attempting to ascertain the risk of a landslide  
 281 occurring in a given area.

282       The aforementioned elevation difference provides the sliding main body material  
 283 with a relatively large distance over which to convert potential energy to kinetic energy.  
 284 By the time the slide collides with the landscape after experiencing gravitational  
 285 acceleration, the maximum speed of the landslide could exceed 20 m/s. Due to the  
 286 presence of rock mass discontinuities and the variable slide speeds within the landslide  
 287 mass, the slide destroys any new material it encounters and erodes the surrounding rock  
 288 and soil as it enters the scraping zone.

289       During the impact scraping stage, the leading edge of the Sliding main body Impacts

290 the underlayer at a high speed. This impact imparts a certain amount of kinetic energy to  
291 the underlayer, which merges into the slide and increases its total volume. The formation  
292 of a grain rolling friction zone in the boundary layer promotes longer landslide runouts.  
293 Eventually, the kinetic energy of the slide weakens to the point where it can no longer  
294 damage the underlayer. At this time, the landslide transitions from the impact scraping  
295 stage to the debris deposition stage.

296 After the scraping stage, the landsliding main body material continues to  
297 disintegrate, and the grain size further decreases. During debris deposition, large slide  
298 blocks are left in the uppermost depositional layers at the slope toe, while smaller slide  
299 blocks are buried more deeply at the leading edge of the slide. Eventually, frictional  
300 forces cause the kinetic energy of the slide to dissipate, and the mobility of the slide  
301 stops.

302 *4.2. Landslide mobility indices*

303 Based on preliminary analyses of our field data, as well as other previously  
304 published data, we identified fifteen high-position and long-runout landslides with typical  
305 scraping characteristics, ten of which are located in southwest China and five of which  
306 reside in other countries (Table 2). These landslides each have a volume of more than  
307 200,000 m<sup>3</sup>, an equivalent coefficient of friction of less than 0.33, and a scraping ratio  
308 ( $E_R = V_E/V_T$ ,  $V_E$  is the volume of the underlayer material) of greater than 0.2. We  
309 conducted statistical analyses on the characteristics of these fifteen landslides.

310 **Table 2**

311 Characteristics of typical high-position landslides.

---

Landslide name	$V_M (10^4 \text{ m}^3)$	$V_E (10^4 \text{ m}^3)$	$V_T (10^4 \text{ m}^3)$	H (m)	H/L ratios	$E_R$	Source
----------------	--------------------------	--------------------------	--------------------------	-------	------------	-------	--------

---

Touzhai	1200	300	1500	3650	0.26	0.3	Xing et al., 2016
Niumiangou	380	200	580	3000	0.3	0.5	Zhang et al., 2013
Donghekou	500	400	900	2400	0.29	0.8	Yin, 2009
Jiweishan	500	80	580	2200	0.29	0.2	Yin et al., 2011
Guanling	98.5	61	159.5	1400	0.31	0.6	Xing et al., 2014
Zhaojiagou	20	10	30	900	0.28	0.5	Yin et al., 2017
Sanxicun	27.5	11.9	39.4	1200	0.33	0.4	Yin et al., 2016
Xianchi reservoir	144	30	174	1500	0.26	0.2	Field survey
Zhangjiawan	49	33	82	800	0.33	0.7	Fan et al., 2019
Shuicheng “7.23”	70	80	150	1340	0.32	1.1	Gao et al., 2020
Nevado Huascarán	750	4300	5050	15000	0.27	5.7	Evans et al., 2009
Mount Ontake	3400	1350	4750	13000	0.12	0.4	Oyagi, 1984
Nomash River	30	36	66	2200	0.25	1.2	Hungr et al., 2004
Zymoetz River valley	72	50	122	3000	0.3	0.7	McDougall and Hungr, 2005
Leyte Island	920	400	1320	3800	0.22	0.4	Evans et al., 2007

312 There is a strong positive correlation between the total volume of the landslide ( $V_T$ )  
 313 and the landslide mobility distance (Fig. 5a). While the correlation between  $V_T$  and the

equivalent coefficient of friction is very weak, the overall trend indicates that these two parameters are inversely proportional to one another (Fig. 5b). The correlation between the main landslide volume ( $V_M$ ) and the mobility distance is also poor, but the overall trend indicates that higher  $V_M$  values leads to longer mobility distances (Fig. 5c). Lastly,  $V_M$  exhibits a strong positive correlation with the equivalent coefficient of friction (Fig. 5d), a result that is consistent with those of previously published studies.

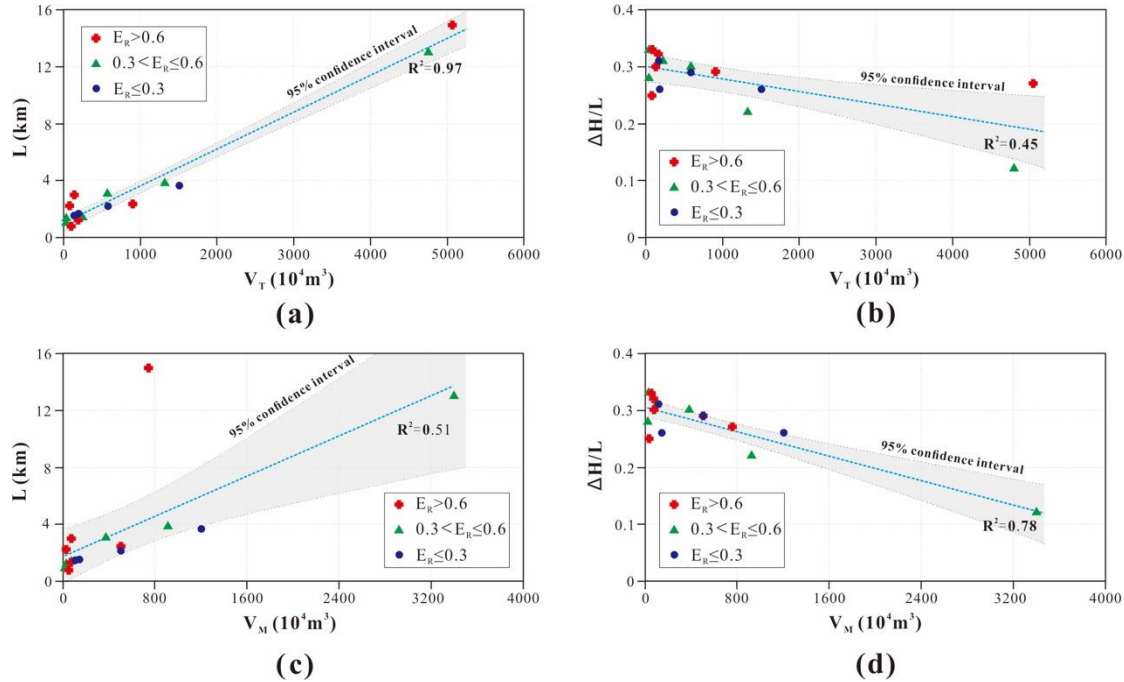


**Fig. 5.** (a) The relationship between the landslide total volume ( $V_T$ ) and the travel distance ( $L$ ). (b) The relationship between the landslide total volume ( $V_T$ ) and the  $\Delta H/L$  number. (c) The relationship between the main landslide volume ( $V_M$ ) and the travel distance ( $L$ ). (d) The relationship between the main landslide volume ( $V_M$ ) and the  $\Delta H/L$  number. Shaded areas represent the 95% confidence interval for the best-fitting trend lines.

The correlation between  $V_T$ , which includes the eroded volume ( $V_s$ ), and the mobility distance is much stronger than it is between  $V_M$  and the mobility distance. As

such, the inclusion of  $V_s$  can lead to more accurate landslide mobility distance estimates in a hazardous risk assessment. It is worth noting that when the scraping ratio is greater than 0.3 but less than 0.6, several points fall outside the 95% confidence interval of the linear relationship between  $V_T$  and the landslide mobility distance. These poor predictions occur because when the scraping ratio is high, the scraping effect has a significant impact on the energy dissipation of the slide and therefore on the mobility distance. Similarly, when the scraping ratio is small,  $V_T$  does not change drastically because little material is added to the initial landslide volume.

## 5. Numerical simulations of landslide scraping dynamics and mobility

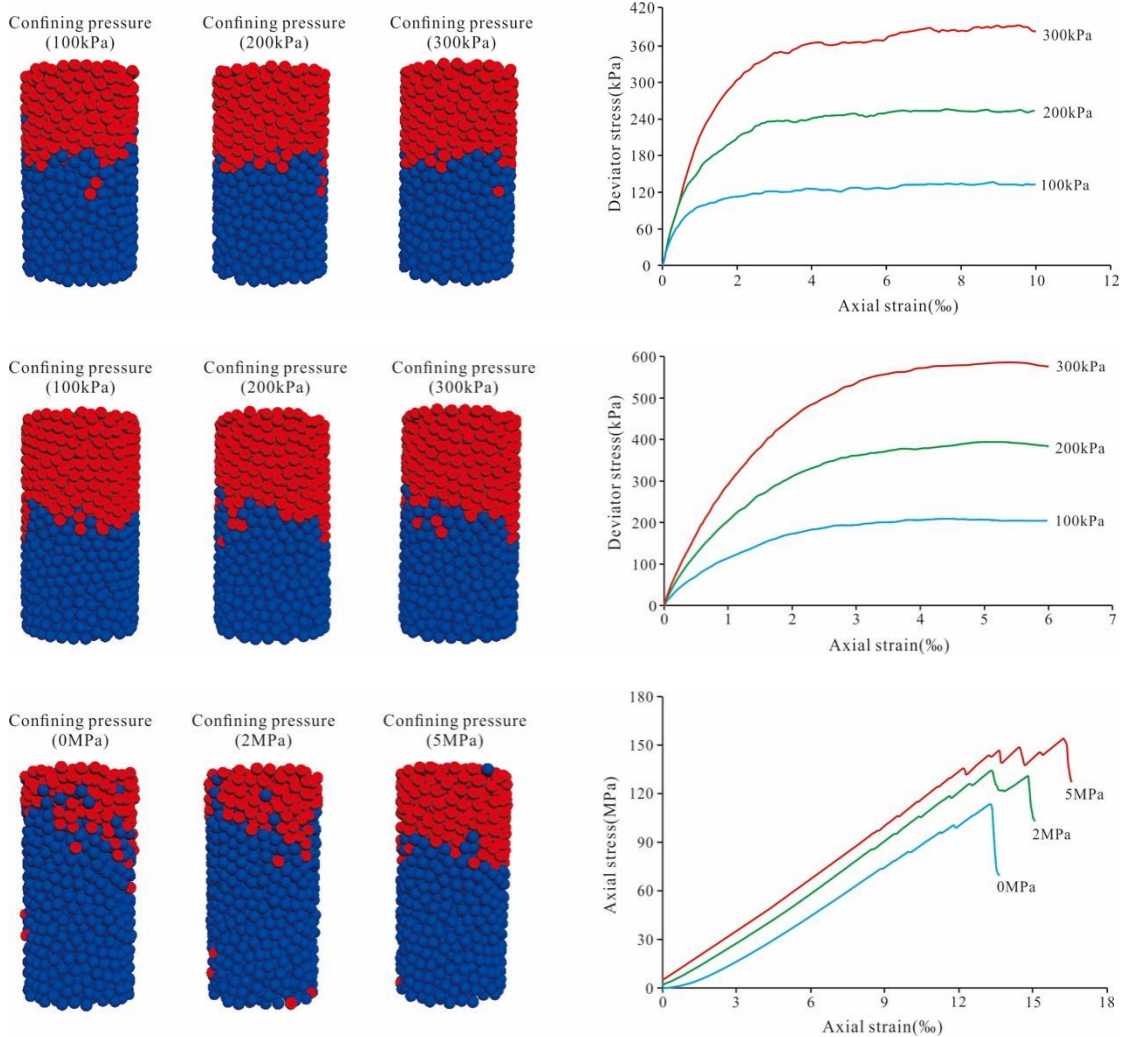
### 5.1. Parameter calibration

In our numerical triaxial tests, we maintained a constant confining pressure during the loading process by controlling the expansion and contraction of the radius of the cylindrical wall. From these tests, we determined possible damage scenarios, stress-strain curves, and the physical and mechanical parameters (e.g., density, cohesion ( $c$ ), and internal friction angle ( $\varphi$ )) for the three erodible underlayers (Fig. 6). The red and blue grains were loaded at opposite ends of the cylinder and then forced to migrate downwards and upwards, respectively. The boundary between the two grain colors represents the fracture surface of the material. The material properties were determined using the stress-strain curve, as defined by different confining pressures, and the Mohr-Coulomb strength criterion. The  $c$  and  $\varphi$  values of the material are defined as:

$$\tan\varphi = \frac{(\sigma_1^{(a)} - \sigma_3^{(a)}) - (\sigma_1^{(b)} - \sigma_3^{(b)})}{(\sigma_1^{(a)} + \sigma_3^{(a)}) - (\sigma_1^{(b)} + \sigma_3^{(b)})} \quad (1)$$

$$2c = \frac{(\sigma_1^a - \sigma_3^a)}{\tan\varphi} - (\sigma_1^a - \sigma_3^a) \quad (2)$$

349 where (a) and (b) represent different confining pressures, and  $\sigma_1$  and  $\sigma_3$  are the maximum  
 350 and minimum principal stresses, respectively, in the Mohr-Coulomb constitutive model.



351 **Fig. 6.** Shear fracture characteristics and stress-strain curves for (a) underlayer I  
 352 (saturated residual slope soil), (b) underlayer II (dry residual slope soil), and (c)  
 353 underlayer III (limestone bedrock) due to different confining pressures.

354 Through many experiments, the parameters directly inputted in simulation software  
 355 are obtained when the curve characteristics are close to those of the actual material. And  
 356 through parameter calibration, the mechanical parameter values obtained from the  
 357 numerical triaxial tests (Table 3) are perfectly integrated with the true measured strength

358 parameters of the geotechnical material (Table 4). underlayers I, II, and III, with their  
 359 varying  $c$  and  $\varphi$  values, correspond to saturated residual slope soil, dry residual slope soil,  
 360 and limestone bedrock, respectively (Table 4). underlayer I represents the saturated weak  
 361 erodible material, which exhibits a low effective stress between soil grains and a low  
 362 mechanical strength. underlayer II represents the hard erodible material, which exhibits a  
 363 high effective stress between soil grains and a high mechanical strength. Lastly,  
 364 underlayer III represents the hard bedrock erodible material, which has a high mechanical  
 365 strength.

366 **Table 3**

367 Underlayer material parameters for our numerical chute test simulations.

Numerical material	Real material	Poisson's ratio	Shear modulus (Pa)	Density (kg·m <sup>-3</sup> )	grain size (m)	Contact radius (m)	Coefficient of restitution	Coefficient of friction
Sliding Limestone								
main body	debris	0.23	$4.77 \times 10^{10}$	2600	0.2	0.2	0.73	0.4
I	grains							
underlayer I	Saturated residual	0.3	$4.46 \times 10^7$	1600	0.2	0.2	0.25	0.1
	slope soil							
underlayer II	Dry residual	0.3	$6.38 \times 10^7$	1900	0.2	0.2	0.25	0.4
	slope soil							

		Poisson's ratio	Shear modulus (Pa)	Density ( $\text{kg}\cdot\text{m}^{-3}$ )	grain size (m)	Contact radius (m)	Coefficient of restitution	Contact Coefficient of friction
Sliding main body	Limestone bedrock	0.23	$4.77\times 10^{10}$	2600	0.2	0.2	0.73	0.4
II			Contact normal stiffness ( $\text{GN}\cdot\text{m}^{-1}$ )		Contact tangential stiffness ( $\text{GN}\cdot\text{m}^{-1}$ )		Critical normal stress (MPa)	Critical shear stress (MPa)
				30	15	340	170	
underlayer	Limestone bedrock	0.23	$4.77\times 10^{10}$	2600	0.2	0.2	0.73	0.4
III			Contact normal stiffness ( $\text{GN}\cdot\text{m}^{-1}$ )		Contact tangential stiffness ( $\text{GN}\cdot\text{m}^{-1}$ )		Critical normal stress (MPa)	Critical shear stress (MPa)
				30	15	340	170	

368 **Table 4**

369 Observed underlayer material parameters.

Numerical material	Real material	Density	Poisson's ratio	Cohesion (kPa)	Internal friction angle (°)	Compressive Strength (kPa)

---

	Saturated						
underlayer I	residual slope soil	1600	0.3	3.39	21.78	—	—
underlayer II	Dry residual slope soil	1900	0.3	6.35	29.33	—	—
underlayer III	Limestone bedrock	2600	0.23	$2 \times 10^4$	48.59	$1.14 \times 10^5$	

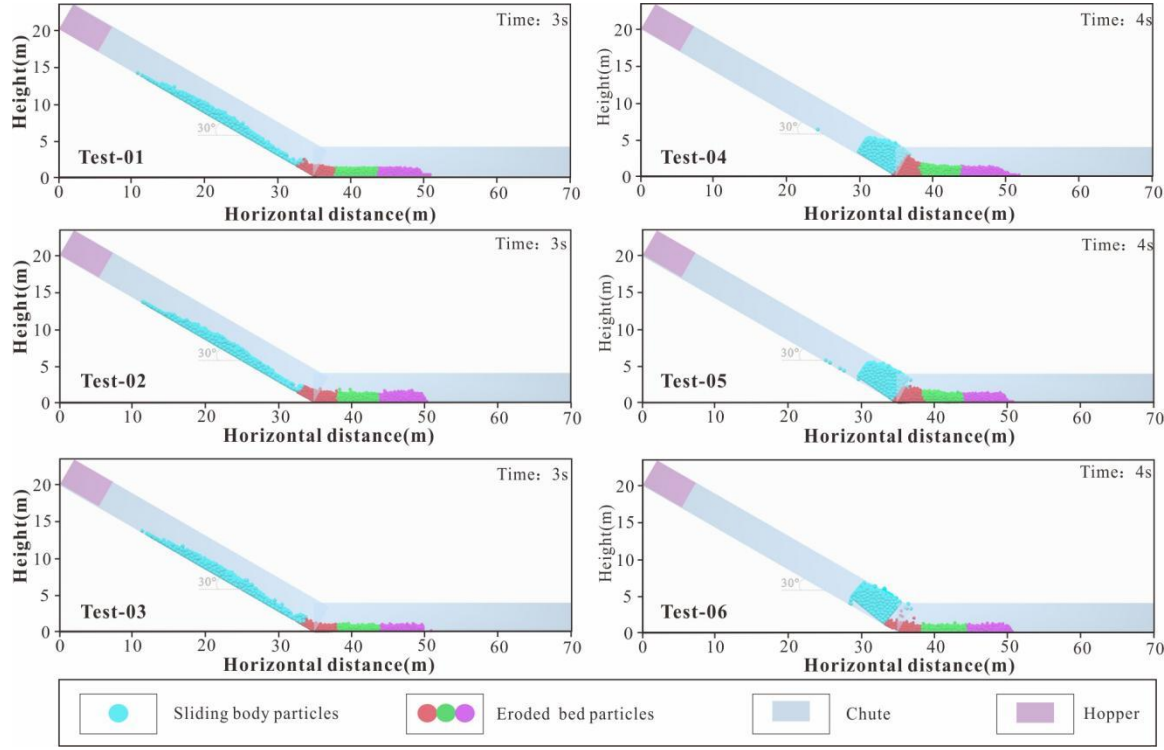
---

370     *5.2. Model results*

371       We conducted a total of six numerical simulations, each with a mobility simulation  
 372 period of 9 s. The underlayer is divided into red, green, and pink sections, and the  
 373 original sliding main body material (either grains or a solid limestone block) is blue.  
 374 Based on our observations, we identified three mobility stages: the initial contact stage,  
 375 the impact scraping stage, and the final deposition stage.

376       The initial contact stage of six tests are shown in Fig. 7. Differences in the physical  
 377 properties of the sliding main body material and the underlayer material result in distinct  
 378 variations in the resulting landslide mobility. Test-01 through Test-03 use a landslide  
 379 load comprised of grains, while Test-04 through Test-06 use a landslide load comprised  
 380 of a limestone block. In Test-01, the impact with the weak underlayer excavates the front  
 381 of the underlayer and shifts those grains toward the bottom of the underlayer. With a  
 382 harder underlayer (Test-02) and a bonded underlayer (Test-03), minimal damage occurs  
 383 at the front of the underlayer, and most of the landsliding main body material is deposited  
 384 on top of the underlayer. For Test-04 through Test-06, the limestone block moves slower  
 385 than the debris grain material material, and only starts to encounter the underlayer after 4

386 s. In the presence of the weak underlayer (Test-04), a hard underlayer (Test-05), and a  
 387 bonded underlayer (Test-06), the limestone block imparts little to no damage to the  
 388 underlayer.

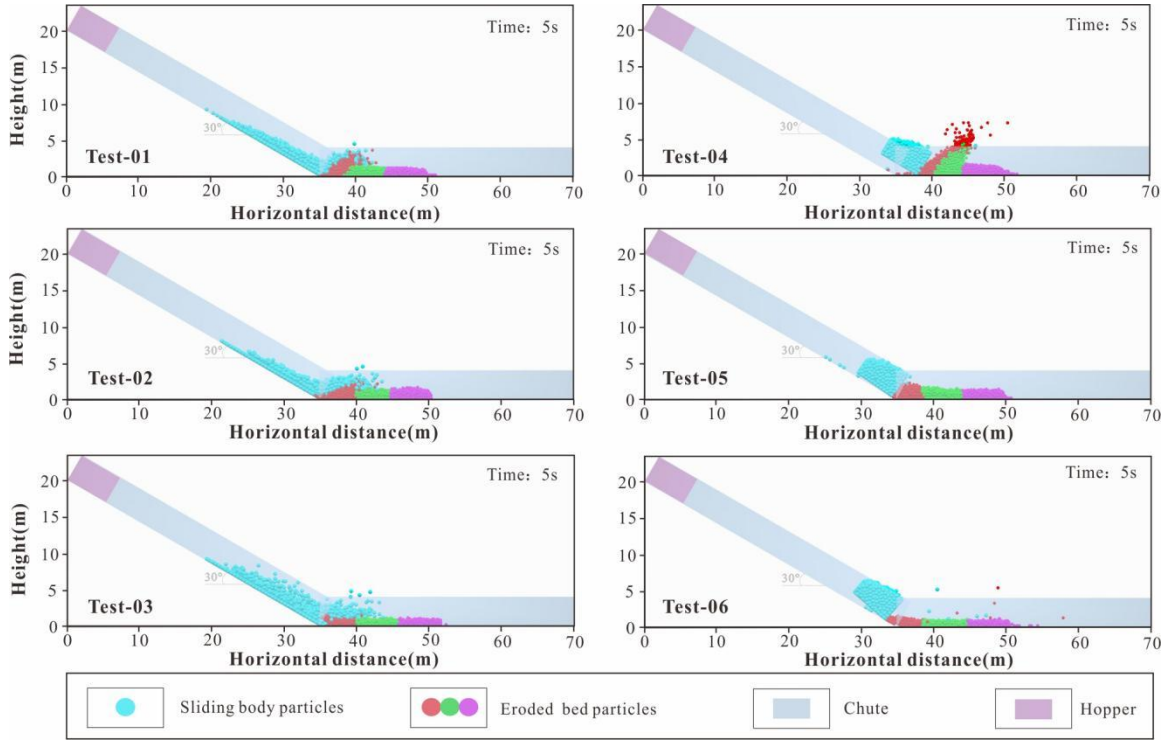


389

390 **Fig. 7.** The initial impact contact stages of the six numerical chute test simulations.

391 The impact scraping stage is shown in Fig. 8. In Test-01, grains at the back of the  
 392 debris grain material continue to push the weak underlayer forward after sliding begins to  
 393 override the underlayer. For the hard underlayer (Test-02), as the sliding rushes over the  
 394 top of the underlayer, it also entrains the underlayer, which drives the underlayer into  
 395 shear failure. When the debris grain material encounters the bonded underlayer (Test-03),  
 396 the underlayer stays intact while it is pushed along the chute. When the sliding main body  
 397 material is a limestone block, impact with the weak underlayer (Test-04) results in  
 398 splashing of the underlayer grains. With the hard underlayer (Test-05), only the red part  
 399 of the underlayer experiences significant compression. Again, the bonded underlayer

400 (Test-06) is almost entirely undamaged when it is struck by the limestone block material.

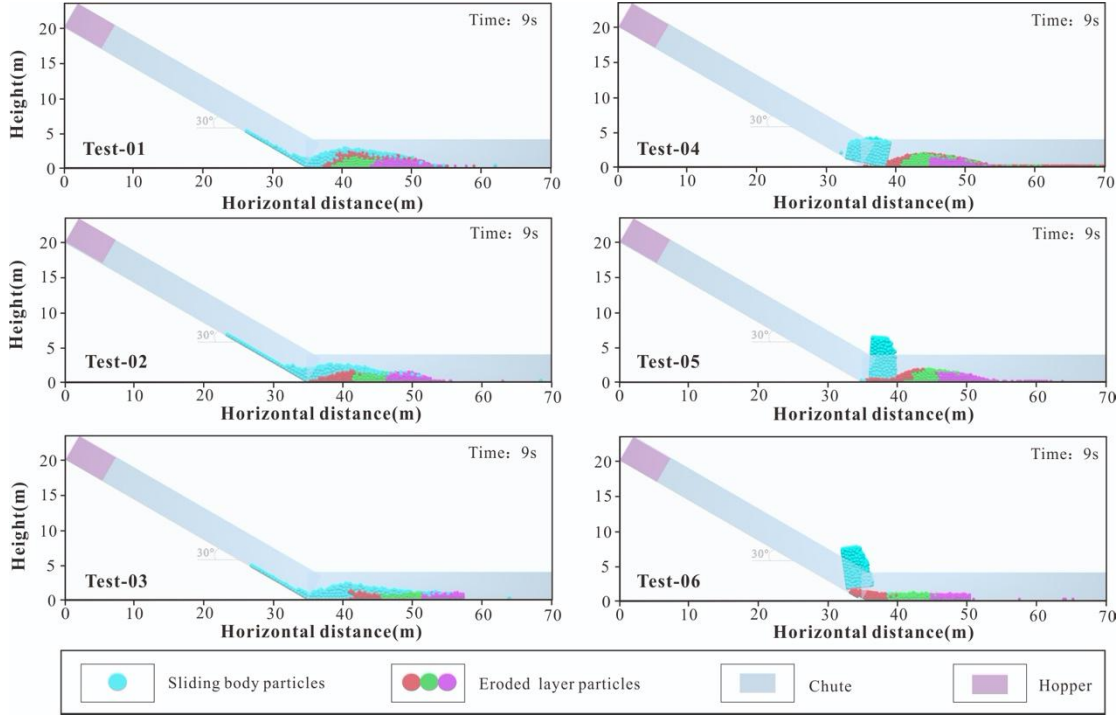


401

402 **Fig. 8.** The impact and scraping stages of the six numerical chute test simulations.

403 At 9 s, the final deposition stage for all six numerical chute simulations begins (Fig.  
 404 9). When the debris grain material impact the weak underlayer (Test-01), all three parts  
 405 of the underlayer experience failure and are pushed along the horizontal chute. In the  
 406 scenario with the hard underlayer (Test-02), the underlayer experiences localized failure  
 407 in the red zone, with little deformation occurring elsewhere in the underlayer. The  
 408 bonded underlayer (Test-03) translates laterally but does not experience any significant  
 409 damage when it is struck by the debris grain material. When the limestone block material  
 410 encounters the weak underlayer (Test-04), the red zone of the underlayer is sprayed away  
 411 from the underlayer, while the green and pink zones experience significant deformation.  
 412 Similarly, when the limestone block material strikes the hard underlayer (Test-05), the  
 413 kinetic energy pushes the underlayer forward as a whole, while also internally deforming

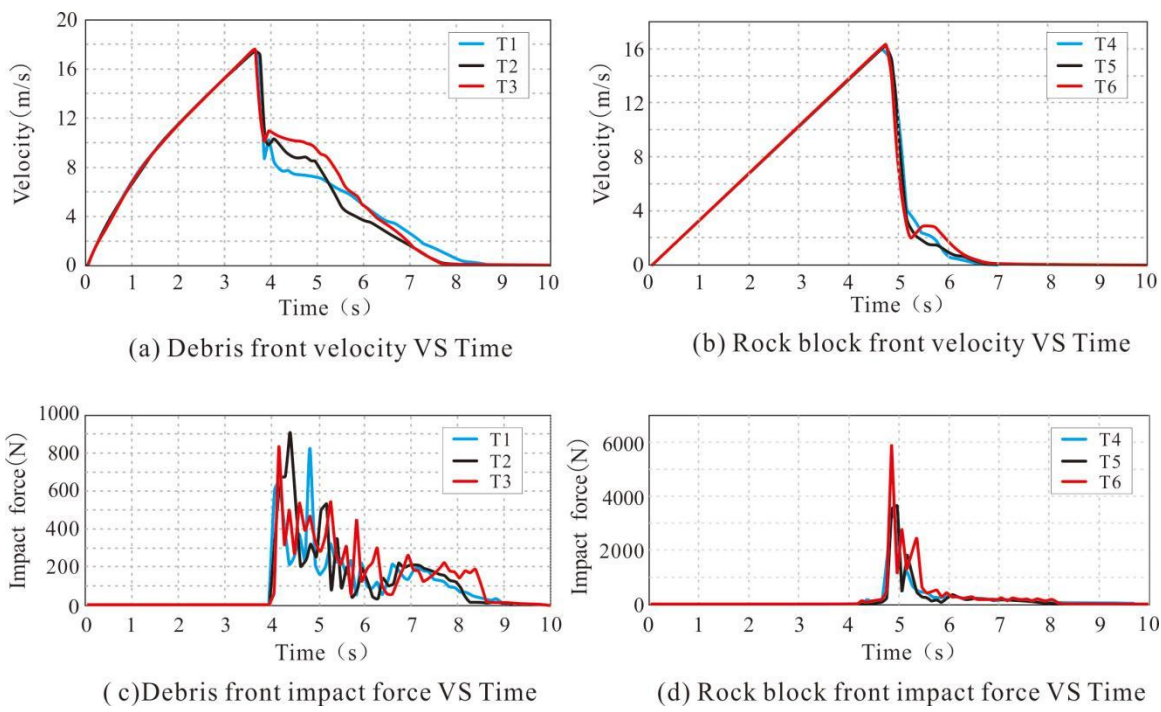
414 the underlayer itself. Despite the impact of the limestone block, the bonded underlayer  
 415 (Test-06) neither moves nor deforms.



416  
 417 **Fig. 9.** The final deposition stages of the six numerical chute test simulations.

418 Depending on the velocity comparison ([Fig.10 \(a\) and \(b\)](#)), debris grain material  
 419 moves faster than the limestone block material, with a maximum velocity of 17.5m/s,  
 420 indicating greater mobility of landslide-debris flow. During the contact between debris  
 421 grain material and underlayer, the underlayer of hard material makes the velocity  
 422 decrease of the sliding main body is smaller to compared with the underlayer of weak  
 423 material. Velocity of debris grain material drops to 11m/s after impact contact with  
 424 underlayer of hard material, and velocity of limestone block material drops to 8m/s. This  
 425 phenomenon shows that the debris grain material consumes more energy during contact  
 426 with the underlayer of weak material, and the impact scraping effect is more obvious.  
 427 Velocity of rock block is not different with underlayer. [Fig.10 \(c\) and \(d\)](#) show the

428 impact force of limestone block material is 4-5 times that of debris grain material. Rock  
 429 block avalanche is more destructive to underlayer than debris avalanche. At the same  
 430 time, the impact contact time between the debris grain material and underlayer is longer  
 431 than the limestone block material, indicating that the impact scraping effect is more  
 432 strongly. The scraping effect acts more strongly on the mobility state modification of the  
 433 debris avalanche.

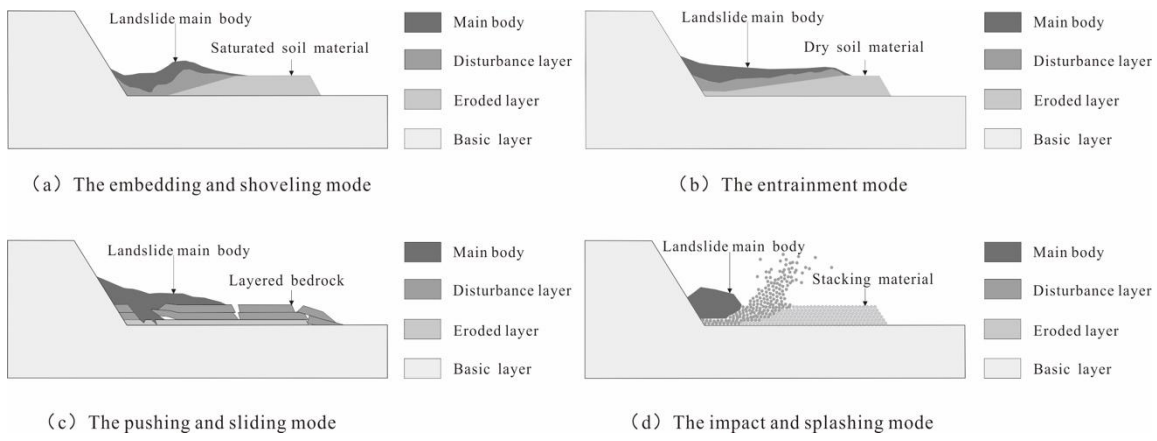


434 Fig. 10. Front velocity and impact force of sliding main body over time curve diagram  
 435

## 436 6. Discussion

437 There are two ways in which the impact scraping of landslides causes the failure of  
 438 the underlay material. In the first scenario, when the leading and side edges of the solid  
 439 slide are moving at high speeds, the underlayer material fails due to vertical impact. In  
 440 the second scenario, material in the boundary layer at the bottom of the slide fails due to  
 441 tangential shearing scraping. Based on a review of previously published works and on

442 data gathered during our field surveys of high-position landslides in Southwest  
 443 mountainous areas, China, we discuss the impact scraping modes of high-position  
 444 landslides through the lens of underlayer scraping. Depending on the sliding main body  
 445 material and the underlayer materials, we classified each high-position landslide as  
 446 falling into one of four impact scraping modes (Fig. 10).



447 (a) The embedding and shoveling mode (b) The entrainment mode  
 448 (c) The pushing and sliding mode (d) The impact and splashing mode

449

450

**Fig. 10.** The four impact scraping modes of high-position and long-runout landslides: (a) the embedding and excavation mode, (b) the entrainment mode, (c) the pushing and sliding mode, and (d) the impact and splashing mode.

451 (1) The embedding and excavation mode (Fig. 10a): During the initial collision of  
 452 the landslide and the weak underlayer, the leading edge of the Sliding main body Is  
 453 driven into the underlayer through plastic deformation. Due to the large amount of kinetic  
 454 energy present, the remaining sliding main body material is thrust over the top of the  
 455 underlayer. The embedded part of the slide damages the underlayer and forces it to  
 456 translate laterally for some distance. Examples of landslides with this type of impact  
 457 scraping mode include the Zhaojiagou landSliding main body In Zhenxiong, Yunnan,  
 458 China (Yin et al., 2017) and the Frank landSliding main body In Canada (Hung and  
 459 Evans, 2004).

460       (2) The entrainment mode (Fig. 10b): When the underlayer is saturated, it is prone to  
461       entrainment and shearing at the bottom boundary layer of the landslide mobility path. By  
462       adding these scoured materials to the landslide volume, both the runout and the scale of  
463       the disaster increase dramatically. An example of a landslide with the entrainment impact  
464       scraping mode is the Shuicheng “7.23” landSliding main body In Guizhou, China ([Gao et](#)  
465       al., 2020).

466       (3) The pushing and sliding mode (Fig. 10c): In this scenario, the underlayer  
467       consists of large layers of poorly consolidated clastic and clay rocks (e.g., clay-shale),  
468       and there are minimal obstructions located at the front of the underlayer. After the  
469       leading edge of the slide strikes the underlayer, the underlayer initially experiences brittle  
470       failure before the entire underlayer is incorporated into the moving landsliding main body  
471       material. An example of a landslide characterized by the pushing and sliding impact  
472       scraping mode is the Zhangjiawan landSliding main body In Nayong Guizhou, China  
473       ([Fan et al., 2019](#)).

474       (4) The impact and splashing mode (Fig. 10d): With a relatively rigid and durable  
475       underlayer, the kinetic energy of the leading edge of the landsliding main body material  
476       is quickly transmitted to the underlayer material, causing it to disintegrate. The remaining  
477       underlayer material that has not been thrown by the impact is incorporated into the  
478       landsliding main body material. Examples of landslides characterized by the impact and  
479       splashing scraping mode include the Jiguanling landslide ([Wang et al., 2014](#)) and the  
480       Jiweishan landslide ([Gao et al., 2016](#)), both of which occurred in Wulong, Chongqing,  
481       China.

482

483     **7. Conclusion**

484       Impact scraping in high-position landslide dynamics influences both the landslide  
485       volume and the overall travel distance of the landslide. Ignoring the effect of impact  
486       scraping may lead to underestimation of the scale of a potential landslide during  
487       hazardous risk assessments. We conducted field surveys, statistical analyses, and  
488       numerical simulations to explore how high-position and long-runout landslides are  
489       altered by impact scraping effect. The results show that different underlayer material and  
490       sliding main body material impact scraping effect has certain regularity. Debris  
491       avalanche has long duration under impact scraping effect, and rock avalanche has strong  
492       impact kinetic energy. Impact scraping effect has strong modification on debris  
493       avalanche. Sliding main body has more obvious impact scraping effect on weak  
494       underlayer

495       There are four evolutionary stages in a high-position and long-runout landslide:  
496       high-position failure shearing, gravitational acceleration, impact scraping, and debris  
497       deposition. The effect of impact scraping vastly increases both the landslide volume and  
498       the risk posed by this natural disaster. When accounting for the effect of impact scraping,  
499       the total landslide volume exhibits a strong positive correlation with the landslide runout  
500       distance. The impact scraping mode, and, consequently, the mobility of a given  
501       high-position landslide, are related to the material properties of the erodible underlayer.  
502       We identified four major impact scraping modes: the embedding and excavation mode,  
503       the entrainment mode, the pushing and sliding mode, and the impact and splashing mode.

504     **Acknowledgments**

505       We acknowledge support from Institute of Geo-Mechanics (DZLXJK201901),

506 National Natural Science Foundation of China (41907257), the National Key Research  
507 and Development Program of China "The Disaster Pattern and Risk Prevention  
508 Technology of Large Landslides in the Karst Mountain Area" (Nos. 2018YFC1504804  
509 and 2018YFC1504806).

510

511 Conflict of Interest:

512 The authors declare that they have no conflict of interest. This article does not contain  
513 any studies with human participants or animals performed by any of the authors.

514 Informed consent was obtained from all individual participants included in the study."

515    **References**

- 516    Bonnard, C., 2004. The meaning of risk assessment related to large landslides, in:  
517         Identification and Mitigation of Large Landslide Risks in Europe: Advances in Risk  
518         Assessment. Balkema Publishers, Leiden, pp. 7–12.
- 519    Brideau, M.-A., Stead, D., Millard, T.H., Ward, B.C., 2019. Field characterisation and  
520         numerical modelling of debris avalanche runout on Vancouver Island, British  
521         Columbia, Canada. *Landslides*, 16, 875–891.  
522         <http://doi.org/10.1007/s10346-019-01141-7>.
- 523    Brunetti, M.T., Guzzetti, F., Cardinali, M., Fiorucci, F., Santangelo, M., Mancinelli, P.,  
524         Komatsu, G., Borselli, L., 2014. Analysis of a new geomorphological inventory of  
525         landslides in Valles Marineris, Mars. *Earth and Planetary Science Letters*, 405,  
526         156–168. <http://doi.org/10.1016/j.epsl.2014.08.025>.
- 527    Corominas, J., 1996. The angle of reach as a mobility index for small and large landslides:  
528         Reply. *Canadian Geotechnical Journal*, 33, 1029–1031.  
529         <http://doi.org/10.1139/t96-131>.
- 530    Crosta, G.B., Imposimato, S., Roddeman, D., 2009. Numerical modelling of  
531         entrainment/deposition in rock and debris-avalanches. *Engineering Geology*, 109,  
532         135–145. <http://doi.org/10.1016/j.enggeo.2008.10.004>.
- 533    Crozier, M.J., 1986. *Landslides: Causes, Consequences Environment*. Croom Helm Pub.,  
534         London, 245..
- 535    Crozier, M.J., Glade, T., 2012. Landslide hazard and risk: issues, concepts and approach.  
536         *Landslide Hazard and Risk*, 1–40.
- 537    Cundall, P.A., 1971. A computer model for simulating progressive large-scale mobilitys

538 in blocky rock systems, in: Proceedings of the Symposium of the International  
539 Society for Rock Mechanics. Society for Rock Mechanics (ISRM), France, II-8.

540 Cundall, P.A., Strack, O.D.L., 1979. A discrete numerical model for granular assemblies.  
541 Géotechnique, 29, 47–65. <http://doi.org/10.1680/geot.1979.29.1.47>.

542 Dufresne, A., 2012. Granular flow experiments on the interaction with stationary runout  
543 path materials and comparison to rock avalanche events. Earth Surface Processes and  
544 Landforms, 37, 1527–1541. <http://doi.org/10.1002/esp.3296>.

545 Evans, S.G., Bishop, N.F., Fidel Smoll, L., Valderrama Murillo, P., Delaney, K.B.,  
546 Oliver-Smith, A., 2009. A re-examination of the mechanism and human impact of  
547 catastrophic mass flows originating on Nevado Huascarán, Cordillera Blanca, Peru in  
548 1962 and 1970. Engineering Geology, 108, 96–118. <http://doi.org/10.1016/j.enggeo.2009.06.020>.

550 Evans S. G., Guthrie R. H., Roberts N. J., Bishop N. F, 2007. The disastrous 17 February  
551 2006 rockslide-debris avalanche on Leyte Island, Philippines: a catastrophic  
552 landsliding main body in tropical mountain terrain. Natural Hazards and Earth  
553 System Science, 7(60). <http://doi.org/10.5194/nhess-7-89-2007>.

554 Fan, X., Xu, Q., Scaringi, G., Zheng, G., Huang, R., Dai, L., Ju, Y., 2019. The “long”  
555 runout rock avalanche in Pusa, China, on August 28, 2017: a preliminary report.  
556 Landslides, 16, 139–154. <http://doi.org/10.1007/s10346-018-1084-z>.

557 Gao, Y., Li, B., Gao, H., Chen, L., Wang, Y., 2020. Dynamic characteristics of  
558 high-elevation and long-runout landslides in the Emeishan basalt area: a case study  
559 of the Shuicheng “7.23” landsliding main body in Guizhou, China. Landslides, 17,  
560 1663–1677. <http://doi.org/10.1007/s10346-020-01377-8>.

- 561 Gao, Y., Li, B., Wang, G.Z., 2016. Motion feature and numerical simulation analysis of  
562 Jiweishan landslide with rapid and long run-out. *Journal of Engineering Geology*, 24,  
563 425–434.
- 564 Guzzetti, F., Ardizzone, F., Cardinali, M., Rossi, M., Valigi, D., 2009. Landslide volumes  
565 and landslide mobilization rates in Umbria, central Italy. *Earth and Planetary Science  
566 Letters*, 279, 222–229. <http://doi.org/10.1016/j.epsl.2009.01.005>.
- 567 Heim, A., 1932. Bergsturz und menschenleben. *Naurforschenden Gesellschaft*, Zurich,  
568 Switzerland.
- 569 Hertz, H., 1882. On the contact of elastic solids. Macmillan and Co., New York, 92,  
570 156–171.
- 571 HsÜ, K.J., 1975. Catastrophic debris streams (sturzstroms) generated by rockfalls.  
572 Geological Society of America Bulletin, 86, 129–140.  
573 [http://doi.org/10.1130/0016-7606\(1975\)86<129:cdssgb>2.0.co;2](http://doi.org/10.1130/0016-7606(1975)86<129:cdssgb>2.0.co;2).
- 574 Huang, R., Li, W., 2014. Post-earthquake landsliding and long-term impacts in the  
575 Wenchuan earthquake area, China. *Engineering Geology*, 182, 111–120.  
576 <http://doi.org/10.1016/j.enggeo.2014.07.008>.
- 577 Hungr, O., 2004. Landslide hazards in BC: achieving balance in risk assessment.  
578 Innovation. *Journal of the Association of Professional Engineers and Geoscientists of  
579 BC*, 8, 12–15.
- 580 Hungr, O., Evans, S.G., 2004. Entrainment of debris in rock avalanches: An analysis of a  
581 long run-out mechanism. *Geological Society of America Bulletin*, 116, 1240–1252.  
582 <http://doi.org/10.1130/b25362.1>.
- 583 Iverson, R.M., 2012. Elementary theory of bed-sediment entrainment by debris flows and

- 584 avalanches. Journal of Geophysical Research, 117.
- 585 <http://doi.org/10.1029/2011jf002189>.
- 586 Iverson, R.M., George, D.L., Allstadt, K., Reid, M.E., Collins, B.D., Vallance, J.W.,  
587 Schilling, S.P., Godt, J.W., Cannon, C.M., Magirl, C.S., Baum, R.L., Coe, J.A.,  
588 Schulz, W.H., Bower, J.B., 2015. Landslide mobility and hazards: implications of the  
589 2014 Oso disaster. *Earth and Planetary Science Letters*, 412, 197–208.  
590 <http://doi.org/10.1016/j.epsl.2014.12.020>.
- 591 Iverson, R.M., Reid, M.E., Logan, M., LaHusen, R.G., Godt, J.W., Griswold, J.P., 2011.  
592 Positive feedback and momentum growth during debris-flow entrainment of wet bed  
593 sediment. *Nature Geoscience*, 4, 116–121. <http://doi.org/10.1038/ngeo1040>.
- 594 Legros, F., 2002. The mobility of long-runout landslides. *Engineering Geology*, 63,  
595 301–331. [https://doi.org/10.1016/S0013-7952\(01\)00090-4](https://doi.org/10.1016/S0013-7952(01)00090-4).
- 596 Li, T., 1983. A mathematical model for predicting the extent of a major rockfall.  
597 *Zeitschrift für Geomorphologie*, 27, 473–482.
- 598 Li, T.H., Fan, X.Y., Jiang, Y.J., 2018. Study on equivalent impact force and impact  
599 distribution range of landslide debris flow with different gradation. *Mountain  
600 Research*, 36, 740–749.
- 601 Li, X.L., Tang, H.M., Xiong, C.R., Luo, H.M., 2012. Influence of substrate ploughing  
602 and erosion effect on process of rock avalanche. *Rock and Soil Mechanics*, 33,  
603 1527–1534, 1541.
- 604 Liu, C., Qin, Y., Tang, Q., Le, T.C., 2017. Numerical simulation of compacted failure in  
605 porous sandstone based on discrete element method. *Journal of Guilin University of  
606 Technology*, 37, 536–540.

- 607 Lucchitta, B.K., 1978. A large landslide on mars. Geological Society of America Bulletin,  
608 89, 1601–1609. [http://doi.org/10.1130/0016-7606\(1978\)89<1601:allom>2.0.co;2](http://doi.org/10.1130/0016-7606(1978)89<1601:allom>2.0.co;2).
- 609 Malamud, B.D., Turcotte, D.L., Guzzetti, F., Reichenbach, P., 2004. Landslides,  
610 earthquakes, and erosion. Earth and Planetary Science Letters, 229, 45–59.  
611 <http://doi.org/10.1016/j.epsl.2004.10.018>.
- 612 Mangeney, A., Roche, O., Hungr, O., Mangold, N., Faccanoni, G., Lucas, A., 2010.  
613 Erosion and mobility in granular collapse over sloping beds. Journal of Geophysical  
614 Research, 115. <http://doi.org/10.1029/2009jf001462>.
- 615 McDougall, S., Hungr, O., 2005. Dynamic modelling of entrainment in rapid landslides.  
616 Canadian Geotechnical Journal, 42, 1437–1448. <http://doi.org/10.1139/t05-064>.
- 617 Mindlin, R.D., 1949. Compliance of elastic bodies in contact. Journal of Applied  
618 Mechanics, 16, 259-268.
- 619 Mindlin, R.D., Deresiewicz, H., 1953. Elastic spheres in contact under varying oblique  
620 forces. ASME, 20, 327-344.
- 621 Oyagi, N., 1987. The 1984 Ontake-san landslide and its mobility. Geomorphological  
622 Union, 8, 127–144.
- 623 Pirulli, M., Pastor, M., 2012. Numerical study on the entrainment of bed material into  
624 rapid landslides. Géotechnique, 62, 959–972. <http://doi.org/10.1680/geot.10.p.074>.
- 625 Potyondy, D.O., Cundall, P.A., 2004. A bonded-grain model for rock. International  
626 Journal of Rock Mechanics and Mining Sciences, 41, 1329–1364.  
627 <http://doi.org/10.1016/j.ijrmms.2004.09.011>.
- 628 Roback, K., Clark, M.K., West, A.J., Zekkos, D., Li, G., Gallen, S.F., Chamlagain, D.,  
629 Godt, J.W., 2018. The size, distribution, and mobility of landslides caused by the

- 630        2015 Mw7.8 Gorkha earthquake, Nepal. *Geomorphology*, 301, 121–138.
- 631        <http://doi.org/10.1016/j.geomorph.2017.01.030>.
- 632        Savage, S.B., Hutter, K., 1991. The dynamics of avalanches of granular materials from  
633        initiation to runout. Part I: Analysis. *Acta Mechanica*, 86, 201–223.  
634        <http://doi.org/10.1007/bf01175958>.
- 635        Scheidegger, A.E., 1973. On the prediction of the reach and velocity of catastrophic  
636        landslides. *Rock Mechanics Felsmechanik Mcanique des Roches*, 5, 231–236.  
637        <http://doi.org/10.1007/bf01301796>.
- 638        Shreve, R.L., 1968. The blackhawk landslide. *Geological Society of America Special  
639        Paper*, 108, 47.
- 640        Sovilla, B., Burlando, P., Bartelt, P., 2006. Field experiments and numerical modeling of  
641        mass entrainment in snow avalanches. *Journal of Geophysical Research: Earth  
642        Surface*, 111. <http://doi.org/10.1029/2005jf000391>.
- 643        Stiny, J., Die, M., 1910. Debris Flows. Wagnerschen Universitats, Buchhandlung,  
644        Innsbruck, Austria.
- 645        Strom, A., 2014. Catastrophic Slope Processes in Glaciated Zones of Mountainous  
646        Regions. *Landslides in Cold Regions in the Context of Climate Change*. Springer  
647        International Publishing.
- 648        Takahashi, T., 1978. Mechanical characteristics of debris flow. *Journal of the Hydraulics  
649        Division*, 104, 1153–1169.
- 650        Turner, A.K., Schuster, R.L., 1996. Landslides: investigation and mitigation, in:  
651        Transportation Research Board Special Report, vol. 247. National Research Council,  
652        Washington, D.C., pp. 673.

- 653 Voight, B., Janda, R.J., Glicken, H., Douglass, P.M., 1983. Nature and mechanics of the  
654 Mount St Helens rockslide-avalanche of 18 May 1980. *Géotechnique*, 33, 243–273.  
655 <http://doi.org/10.1680/geot.1983.33.3.243>.
- 656 Wang, G.Z., Li, B., Feng, Z., Xing A.G., 2014. Simulation of the process of the  
657 Jiguanling rock avalanche in Wulong of Chongqing. *Hydrogeology Engineering*  
658 *Geology*, 41, 101–106.
- 659 Wang, Y.H., Gu, S.L., Zhao, J., 2017. Study on numerical simulation of process of  
660 landslide accumulation landslide dam based on DEM. *Structural Engineers*, 33,  
661 105–110.
- 662 Xing, A., Wang, G., Li, B., Jiang, Y., Feng, Z., Kamai, T., 2014. Long-runout mechanism  
663 and landsliding behaviour of large catastrophic landslide triggered by heavy rainfall  
664 in Guanling, Guizhou, China. *Canadian Geotechnical Journal*, 52, 971–981.  
665 <http://doi.org/10.1139/cgj-2014-0122>.
- 666 Xing, A., Wang, G., Yin, Y., Tang, C., Xu, Z., Li, W., 2016. Investigation and dynamic  
667 analysis of a catastrophic rock avalanche on September 23, 1991, Zhaotong, China.  
668 *Landslides*, 13, 1035–1047. <http://doi.org/10.1007/s10346-015-0617-y>.
- 669 Xu, Q., Huang, R., Yin, Y., Hou, S., Dong, X., Fan, X., Tang, M., 2009. The Jiweishan  
670 landslide of June 5, 2009 in Wulong, Chongqing characteristic and failure  
671 mechanism. *Journal of Engineering Geology*, 17, 433–444.
- 672 Yin, Y., Cheng, Y., Liang, J., Wang, W., 2016. Heavy-rainfall-induced catastrophic  
673 rockslide-debris flow at Sanxicun, Dujiangyan, after the Wenchuan Ms 8.0  
674 earthquake. *Landslides*, 13, 9–23. <http://doi.org/10.1007/s10346-015-0554-9>.
- 675 Yin, Y., Sun, P., Zhang, M., Li, B., 2011. Mechanism on apparent dip sliding of oblique

- 676 inclined bedding rockslide at Jiweishan, Chongqing, China. Landslides, 8, 49–65.
- 677 <http://doi.org/10.1007/s10346-010-0237-5>.
- 678 Yin, Y., Xing, A., Wang, G., Feng, Z., Li, B., Jiang, Y., 2017. Experimental and numerical  
679 investigations of a catastrophic long-runout landSliding main body In Zhenxiong,  
680 Yunnan, southwestern China. Landslides, 14, 649–659. <http://doi.org/>  
681 [10.1007/s10346-016-0729-z](https://doi.org/10.1007/s10346-016-0729-z).
- 682 Yin, Y.P., 2009. Rapid and long-runout features of landslides triggered by the wenchuan  
683 earthquake. Journal of Engineering Geology, 17, 153–166.
- 684 Yin, Y.P., 2010. Mechanism of apparent dip slide of inclined bedding rockslide—a case  
685 study of Jiweishan rockSliding main body In Wulong, Chongqing. Chinese Journal  
686 of Rock Mechanics and Engineering, 29, 217–226.
- 687 Yin, Y.P., Wang W.P, Zhang N, Yan J.K, Wei Y.J, Yang L.W. 2017. Long runout  
688 geological disaster initiated by the ridge-top rockSliding main body In a strong  
689 earthquake area: A case study of the Xinmo landSliding main body In Maoxian  
690 County, Sichuan Province. Geology in China, 44(5): 827-841
- 691 Zhang, L., Tang, H.M., Xiong, C.R., Huang, L., Zou Z.X., 2012. mobility process  
692 simulation of high-speed long-distance Jiweishan landslide with PFC3D. Chinese  
693 Journal of Rock Mechanics and Engineering, 31, 2601–2611.
- 694 Zhang Y.S., Cheng Y.L., Yin Y.P., Lan H.X., 2014. High-position debris flow: a long-term  
695 active geohazard after the wenchuan earthquake. Engineering Geology, 180(180):  
696 45-54.
- 697 Zhang, M., Wu, L., Zhang, J., Li, L., 2019. The 2009 Jiweishan rock avalanche, Wulong,  
698 China: deposit characteristics and implications for its fragmentation. Landslides, 16,

- 699 893–906. <http://doi.org/10.1007/s10346-019-01142-6>.
- 700 701 702 703 704 705 706 707 708 709 710 711 712 713 714 715 716 717 718 719 720 721 Zhang, Y., Cheng, Y., Yin, Y., Lan, H., Wang, J., Fu, X., 2014. High-position debris flow: A long-term active geohazard after the Wenchuan earthquake. *Engineering Geology*, 180, 45–54. <http://doi.org/10.1016/j.enggeo.2014.05.014>.
- Zhou, J.-W., Cui, P., Hao, M.-H., 2016. Comprehensive analyses of the initiation and entrainment processes of the 2000 Yigong catastrophic landSliding main body In Tibet, China. *Landslides*, 13, 39–54. <http://doi.org/10.1007/s10346-014-0553-2>.
- Fan, X., et al., The "long" runout rock avalanche in Pusa, China, on August 28, 2017: a preliminary report. *Landslides*, 2019. 16(1): p. 139-154.
- Dufresne, A., Granular flow experiments on the interaction with stationary runout path materials and comparison to rock avalanche events. *Earth Surface Processes and Landforms*, 2012. 37(14): p. 1527-1541.
- Zhou, J.-w., P. Cui, and M.-h. Hao, Comprehensive analyses of the initiation and entrainment processes of the 2000 Yigong catastrophic landSliding main body In Tibet, China. *Landslides*, 2016. 13(1): p. 39-54.
- Mangeney, A., et al., Erosion and mobility in granular collapse over sloping beds. *Journal of Geophysical Research: Earth Surface*, 2010. 115(F3).
- Potyondy, D.O. and P.A. Cundall, A bonded-grain model for rock. *International Journal of Rock Mechanics and Mining Sciences*, 2004. 41(8): p. 1329-1364.
- Huang, D., Li, Y.Q., Song, Y.X., Xu, Q. & Pei, X.J. 2019. Insights into the catastrophic Xinmo rock avalanche in Maoxian county, China: Combined effects of historical

- 722 earthquakes and landslide amplification. Engineering Geology, 258, doi:  
723 10.1016/j.enggeo.2019.105158.
- 724 Huang, D., Song, Y.X., Ma, G.W., Pei, X.J. & Huang, R.Q. 2018. Numerical modeling of  
725 the 2008 Wenchuan earthquake-triggered Niumiangou landslide considering effects  
726 of pore-water pressure. Bulletin of Engineering Geology and the Environment, doi:  
727 10.1007/s10064-018-01433-7.
- 728 Song, Y., Huang, D. & Cen, D. 2016. Numerical modelling of the 2008 Wenchuan  
729 earthquake-triggered Daguangbao landslide using a velocity and displacement  
730 dependent friction law. Engineering Geology, 215, 50-68, doi:  
731 10.1016/j.enggeo.2016.11.003.